IEEE Photonics Journal
An IEEE Photonics Society Publication

Open Access

Optimized Denoising Method for Fourier Ptychographic Microscopy Based on Wirtinger Flow

Volume 11, Number 1, February 2019

Sining Chen
Tingfa Xu
Jizhou Zhang
Xing Wang
Yizhou Zhang

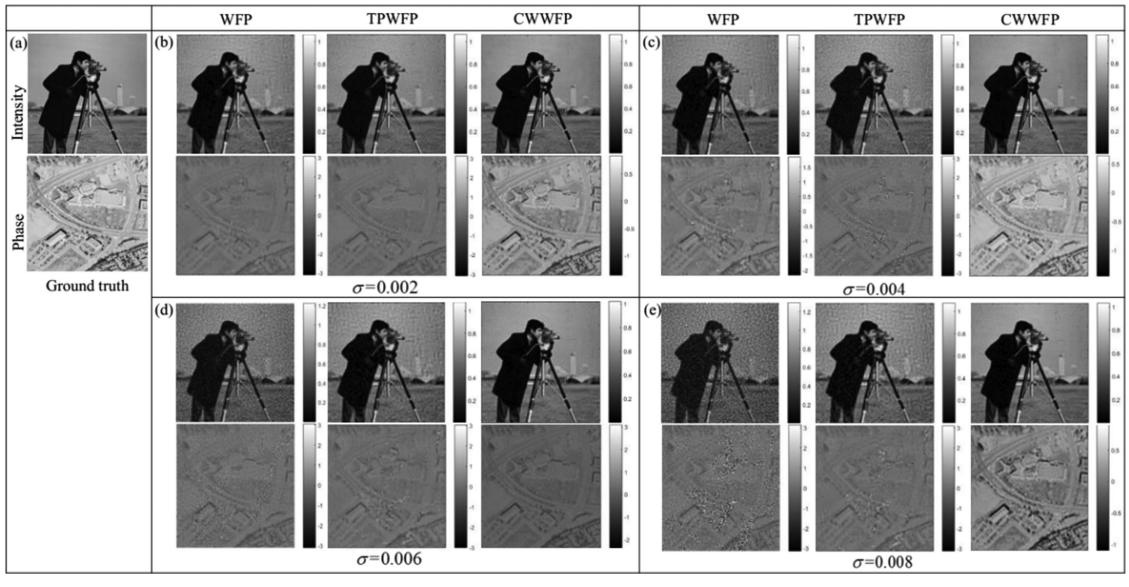

DOI: 10.1109/JPHOT.2019.2890830
1943-0655

IEEE photonics SOCIETY

IEEE

Optimized Denoising Method for Fourier Ptychographic Microscopy Based on Wirtinger Flow

Sining Chen, Tingfa Xu, Jizhou Zhang, Xing Wang, and Yizhou Zhang

School of Optics and Photonics, Beijing Institute of Technology, Beijing 100081, China

DOI:10.1109/JPHOT.2019.2890830

Manuscript received November 19, 2018; revised December 25, 2018; accepted December 31, 2018. Date of publication January 3, 2019; date of current version January 15, 2019. This work was supported in part by the Major Science Instrument Program of the National Natural Science Foundation of China under Grant 61527802, in part by the General Program of National Natural Science Foundation of China under Grant 61371132 and Grant 61471043. Corresponding author: Tingfa Xu (e-mail: ciom_xtf1@bit.edu.cn).

Abstract: Fourier ptychographic microscopy (FPM) is a recently developed technique for high-resolution complex imaging with a wide field-of-view. FPM combines captured low-resolution images corresponding to angle-varying illuminations in the Fourier domain with phase retrieval and synthetic aperture algorithms; consequently, it can surpass the space-bandwidth product limit of an objective lens. In typical FPM systems, the reconstructed result is sensitive to various types of system and environmental noise; thus, the quality can be significantly degraded. In this paper, based on the Wirtinger flow gradient descent framework, we propose an optimized phase retrieval method, which searches for the optimization results with iteratively changing weights and suppresses noise by utilizing captured noise and its corresponding constrained item. A correction term is further introduced into the new algorithm. This method cannot only adapt to varying sampling conditions but also provide an accurate optimum solution. We validate our method with both simulated and experimental images. The reconstructed results all illustrate the effectiveness and robustness of our method and demonstrate that the proposed method can significantly depress noise and improve the reconstruction performance of high-resolution complex images.

Index Terms: Coherence imaging, microscopy, image reconstruction.

1. Introduction

Fourier ptychography (FP) is a recently developed imaging technique aimed at recovering a high-resolution (HR), complex (i.e., with amplitude and phase information) image with a wide field-of-view (FOV) [1], [2]. In contrast to conventional ptychography [3], [4], which uses a removable illumination probe, FP utilizes a light-emitting diode (LED) matrix as the lighting source to obtain different incident angles. Therefore, a series of low-resolution (LR) images corresponding to different spatial spectrum bands of the sample with sufficient overlap are captured without moving an illumination probe with a limited size. Then, these spectrum bands are stitched together sequentially to achieve synthetic aperture imaging [5]–[8], which overcomes physical space-bandwidth-product (SBP) limitations. FP was recently introduced into microscopic imaging; the corresponding technique is known as Fourier ptychographic microscopy (FPM) [9], for which a phase retrieval technique [10]–[12] is applied to recover lost phase information. By utilizing both synthetic aperture and phase retrieval techniques,

FPM reconstructs HR complex images that surpass the diffraction limit of the objective lens [13] and expand the SBP of the microscope. Theoretically, the final resolution is determined by the sum of the objective lens and illumination numerical apertures (NAs); this summation is called synthetic-aperture imaging [14], [15]. Due to its advantages, numerous applications of FPM have been implemented over the past few years [16]–[18] using the traditional alternating projection (AP) algorithm, which updates the objective function between the spatial and Fourier domains iteratively with intensity or pupil constraints. However, although the AP algorithm is widely used, it is sensitive to the presence of noise, which can significantly degrade the reconstructed image quality and limit the application of FPM.

Various investigations have been conducted to improve the original FPM method [19]–[27]. Some of those studies intended to effectively reduce the relatively long acquisition time [19]–[22], while others aimed to significantly improve the accuracy and resolution of the reconstructed results and consequently proposed noise-robust and system aberration correction algorithms [23]–[27]. These improvements have resulted in substantial differences in reconstructed results, and the enhanced algorithms have shown great potential in biomedical applications. More recent studies, aimed to tackle various sources of noises during the experiment, while others adopted other phase retrieval algorithms in FPM [28]–[30]. For example, semidefinite programming (SDP) convex optimization has been applied to phase retrieval, although it exhibits a slow convergence rate [28]. Subsequently, Wirtinger flow optimization [31], a novel phase retrieval method, was proposed as a Wirtinger Fourier ptychography (WFP) scheme to replace the AP algorithm [29], and an FPM reconstruction method known as Fourier ptychography with sparse representation was also proposed [25]. Specifically, WFP is based on the model of Gaussian noise and can control detector noise effectively. However, truncated Poisson Wirtinger Fourier ptychographic reconstruction (TPWFP) technique, which utilizes the Poisson maximum likelihood and truncated gradient scheme has been shown to exhibit a better performance [30]. Most recently, a reweighted gradient-descent optimization scheme has been tested for phase retrieval under different step-sizes [32], nevertheless, this scheme is characterized by a heavy computational cost and a slow convergence. Although each of these methods works well under different conditions, they all have their own limitations. Therefore, it is important to develop an optimized module to correct interference from unknown sources of noise and obtain an optimization result with a faster convergence rate on current FPM platforms.

In this work, we propose an optimized denoising reconstruction method, known as constrained and weighted Wirtinger Fourier ptychography (CWWFP), which introduces a weighted gradient item with a correction term and a noise relaxation constraint into the Fourier ptychographic reconstruction scheme with a Wirtinger gradient descent framework. The proposed CWWFP technique is intended to efficiently suppress Gaussian, Poisson and speckle noise in the FPM system. Owing to the existence of weighted item, CWWFP is equivalent to having an indirect truncation effect if the result is situated far from the optimum. Moreover, the weighted item is adaptively calculated depending on the preceding iteration. In addition, the introduction of a noise relaxation constraint into this reconstruction scheme means that the proposed CWWFP method can provide accurate descent directions while maintaining the ability to suppress pupil misalignment and various sources of noise. Finally, a correction term is also adopted in the framework that can have fine-tune the estimated spatial spectrum. The advantages of the proposed scheme are as follows:

- The adaptively calculated weighted item is equal to a truncated gradient, and thus, a better gradient descent direction can be obtained while searching for the global optimum.
- The employed noise relaxation constraint can more capably handle the above mentioned measurement noise in FPM setups, and thus, a high-quality complex image can be reconstructed. Furthermore, the fine-tuning term can also correct the recovered spatial spectrum slightly.

To demonstrate the robustness of CWWFP, we evaluate several methods in simulations and experiments, the results of which demonstrate that our proposed method outperforms other existing techniques and obtains better reconstructed results under conditions characterized by different types of noises.

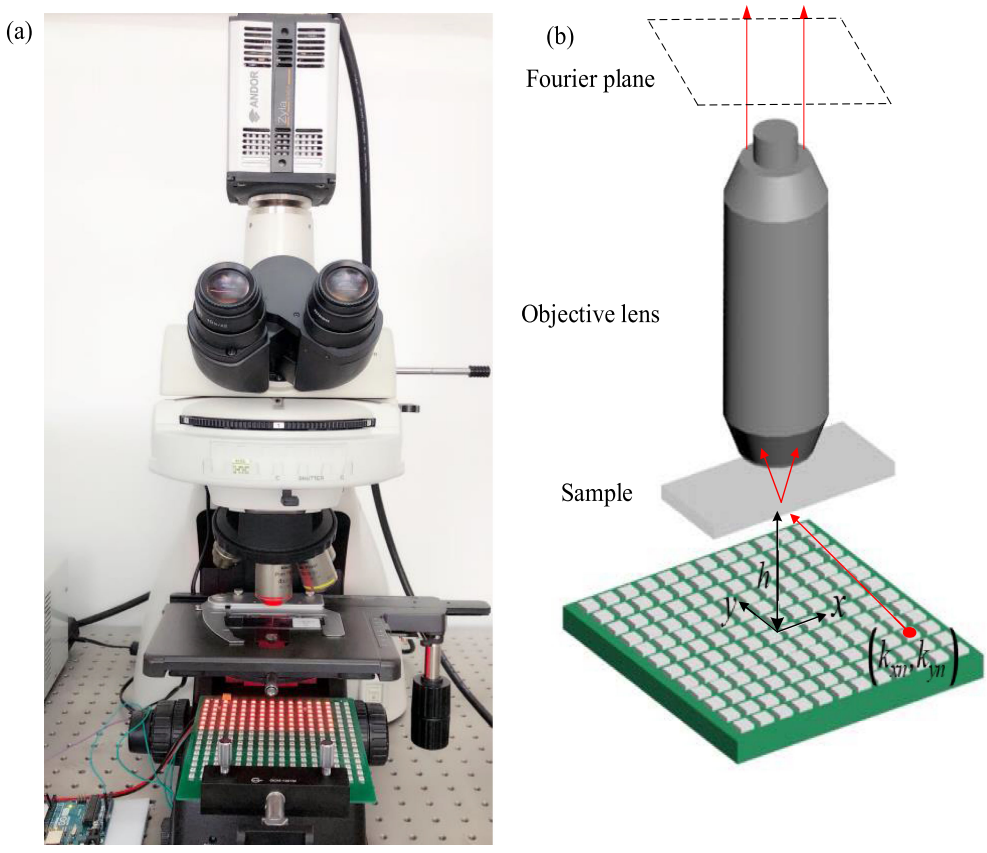

Fig. 1. Experimental setup. (a) The actual experimental setup. (b) The model of the FPM system and the imaging process.

2. Methods

2.1 AP Image Formation

There are two important processes in FPM technique: image acquisition and image reconstruction. As shown in Fig. 1(a), FPM utilizes an LED array source to obtain different oblique illumination plane waves $\mathbf{u}_j = (u_x, u_y)^{\sim}(j = 1, 2, \ldots, N_{img})$ and a complementary metal oxide semiconductor (CMOS) camera to capture the images. The specimen in this system appears thin following the function $O(\mathbf{r})$ in a spatial domain. Fig. 1(b) shows the transmission of the optical path. Because different illumination plane waves correspond to different locations in the Fourier plane, the optical field in the Fourier domain after exiting the specimen is expressed as $O(\mathbf{u} - \mathbf{u}_j)$. Next, the optical field is filtered by the objective pupil $P(\mathbf{u})$, which is equivalent to a low pass filter, and the complex image becomes $\psi_j(\mathbf{u}) = P(\mathbf{u})O(\mathbf{u} - \mathbf{u}_j)$ in the Fourier plane. Then, all of the frequency spectrum information pass through the tube lens and an inverse Fourier transform to reach the imaging sensor. Thus, a set of LR images is captured.

Image reconstruction in the conventional FPM method is an iterative process between the spatial and frequency domains, known as the AP algorithm, which has an initial HR guess in the real-space as

$$E_j(\mathbf{r}) = \left|\mathcal{F}^{-1}\left\{\psi_j(\mathbf{u})\right\}\right|^2, \tag{1}$$

where $E_j(\mathbf{r})$ represents the estimated initial intensity image in the image plane and $\mathcal{F}^{-1}$ is the inverse Fourier transform. Different sub-spectrums corresponding to different illumination angles are synthesized by keeping the phase information unchanged and replacing the estimated amplitudes

with the measured amplitudes $I_j(\mathbf{r})$. This is called the intensity constraint, and it is expressed as

$$\psi^{up}(\mathbf{r}-\mathbf{r}_j)=\sqrt{I_j(\mathbf{r})}\frac{\mathcal{F}^{-1}\left\{\psi_j(\mathbf{u})\right\}}{\sqrt{E_j(\mathbf{r})}}, \tag{2}$$

where $\psi^{up}(\mathbf{r}-\mathbf{r}_j)$ is the updated sub-image. Then this sub-image is transferred to the corresponding frequency region which is then updated as

$$\psi^{up}(\mathbf{u}-\mathbf{u}_j)=P(\mathbf{u})\mathcal{F}\left\{\psi^{up}(\mathbf{r}-\mathbf{r}_j)\right\}. \tag{3}$$

One iteration finishes by repeating this process to all N_{img} sub-regions, and the HR intensity and phase images can be extracted from the entire updated spectrum.

2.2 WF in Ptychography

As stated before, we can regard FPM as a coherent imaging system, the target of which is to reconstruct HR complex images from a sequence of captured LR intensity images. Thus, Eq.1 can be considered a generalized phase retrieval problem.

$$I_j=|\langle\mathbf{A}_j,\mathbf{x}\rangle|^2,\quad j=1,2,\ldots,N_{img}. \tag{4}$$

Here we regard I_j as a series of LR intensity images captured in the spatial domain, $\mathbf{A}_j$ is the corresponding linear transform matrix of the inverse Fourier transform and pupil function, and $\mathbf{x}$ is the HR spatial spectrum recovered from I_j. Based on the quadratic loss function, the WF algorithm simplifies the above formula to minimize the problem as

$$\min_{\mathbf{x}\in C^n}\quad f(\mathbf{x})=\|(\mathbf{A}_j\mathbf{x})^*\odot\mathbf{A}_j\mathbf{x}-I_j\|_F^2,\quad j=1,2,\ldots,N_{img}, \tag{5}$$

where $\|\cdot\|_F$ is the Frobenius norm and $\|\cdot\|_F^2$ is generally used to solve the optimum value. Then, by utilizing the iterative scheme with a Wirtinger gradient descent framework, the WF algorithm can solve the model as follows

$$\mathbf{x}^{k+1}=\mathbf{x}^k-\mu\frac{\partial f}{\partial\mathbf{x}^*}|_{\mathbf{x}=\mathbf{x}^k}, \tag{6}$$

where $\frac{\partial f}{\partial\mathbf{x}^*}$ is the first derivative of $f(\mathbf{x})$, and μ is the gradient descent step size.

In the conventional AP and WFP algorithms, the reconstructed results are easily affected by systematic errors and noise, for example, pupil distortion and even some different types of noise from the LED source or surroundings. In addition, the reconstructed results in WFP can finally converge to a local optimum, and they may correspondingly stagnate within local minimums; as a result, a global optimum cannot be achieved. Therefore, an optimized phase retrieval scheme is important for reconstructing HR complex images.

2.3 CWWFP Scheme for FPM

In this section, a new and updated model is deduced with the introduction of a noise relaxation constraint, a correction term and a weighted item. In consideration of the above mentioned system noise, the measurement formation model based on the high-degree problem in Eq.5 becomes

$$\min_{\mathbf{x}\in C^n}\quad f(\mathbf{x})=\frac{1}{2}\sum_{j=1}^{N_{img}}((\mathbf{A}_j\mathbf{x})^*\odot\mathbf{A}_j\mathbf{x}-I_j+\mathbf{e})^2, \tag{7}$$

where $\mathbf{e}$ represents existing noise, which certainly exists in FPM setups. This noise can vary among each measurement, and it will directly affect the presented intensity. Thus, to incorporate a noise constraint into the measurement function and then optimize $\mathbf{x}$, we introduce a constraint item λ, following which the model can be rewritten as

$$\min_{\mathbf{x}\in C^n}\quad f(\mathbf{x})=\frac{1}{2}\left\|(\mathbf{A}_j\mathbf{x})^2-I_j+\mathbf{e}\right\|_2+\lambda\|\mathbf{e}\|_2,\quad j=1,2,\ldots,N_{img}. \tag{8}$$

Note that λ is a noise constraint item. To solve for the noise model $\mathbf{e}$, we can regard the Eq.8 as a function of $g(\mathbf{e})$ and minimize it as

$$\frac{\partial g(\mathbf{e})}{\partial \mathbf{e}} = (\mathbf{A}_j\mathbf{x})^2 - I_j + \mathbf{e} + \lambda\mathbf{e} = 0. \tag{9}$$

Therefore, the noise relaxation constraint can be expressed as

$$\mathbf{e} = \frac{I_j - (\mathbf{A}_j\mathbf{x})^2}{1+\lambda}, \quad j = 1, 2, \ldots, N_{img}. \tag{10}$$

The numerator term $I_j - (\mathbf{A}_j\mathbf{x})^2$ denotes the difference between the jth measurement and its reconstructed result. Compared with TPWFP, CWWFP assumes a noise item instead of only Poisson distribution; moreover, in terms of FPM reconstruction, CWWFP searches for an optimal solution during the iterative process. Accordingly, we add a weighted item α_j^k to control the gradient descent and solve for the optimization problem. In this method, the weighted item can be regarded as an indirect adaptive truncation. Consequently, We can rewrite Eq.8 as follows:

$$\min_{\mathbf{x}\in C^n} \quad f(\mathbf{x}) = \frac{\alpha_j^k}{2}\left\|(\mathbf{A}_j\mathbf{x})^2 - I_j + \mathbf{e}\right\|_2 + \lambda\|\mathbf{e}\|_2, \quad j = 1, 2, \ldots, N_{img}, \tag{11}$$

where

$$\alpha_j^k = \frac{1}{\left|\left(\mathbf{A}_j\mathbf{x}^k\right)^2 - I_j\right| + \eta}, \quad j = 1, 2, \ldots, N_{img}. \tag{12}$$

In this scheme, the weighted item can be adaptively calculated depending on the estimated value of $\mathbf{x}^{k-1}$, and the composition of recovered image is constantly changing with each iteration. we can see that the corresponding α_j^k will be comparatively low when $\mathbf{A}_j\mathbf{x}$ is close to the optimum one. This small α_j^k will diminish the contribution of $\frac{\partial f}{\partial \mathbf{x}^*}|_{\mathbf{x}=\mathbf{A}_j\mathbf{x}^k}$ to the $\frac{\partial f}{\partial \mathbf{x}^*}$. η is a parameter which can change during the iteration or to be stagnated all the time. Consequently, similar to the truncated parameter in the truncated Wirtinger Fourier (TWF) and TPWFP, techniques, the weighted item can also determine the gradient descent direction. After applying these constraints and optimization, we also adopt a regularization parameter as a fine-tuning item to adjust the estimated spatial spectrum slightly. Hence, Eq.11 can be rewritten as

$$\min_{\mathbf{x}\in C^n} \quad f(\mathbf{x}) = \frac{1}{2}\alpha_j^k\left\|(\mathbf{A}_j\mathbf{x})^2 - I_j + \mathbf{e}\right\|_2 + \lambda\|\mathbf{e}\|_2 + \lambda_1\|\mathbf{x}\|_2, \quad j = 1, 2, \ldots, N_{img} \tag{13}$$

where λ_1 represents a smaller numerical value that slightly controls the spatial spectrum. Furthermore, because the weighted item replaces the judgment of the thresholding constraint, which can also decide whether one measurement is situated far from the reconstruction without adding truncated judgment to each iteration, the convergence will be improved. By combining the above mentioned noise constraint and calculating the partial derivative of $f(\mathbf{x})$ with respect to $\mathbf{x}^*$, we can obtain the minimum of $f(\mathbf{x})$ as

$$\begin{aligned}\frac{\partial f}{\partial \mathbf{x}^*} &= \sum_{j=1}^{N_{img}} \alpha_j^k \mathbf{A}_j^H\left[\left(|\mathbf{A}_j\mathbf{x}|^2 - I_j + \mathbf{e}\right)\odot(\mathbf{A}_j\mathbf{x})\right]|_{\mathbf{x}=\mathbf{x}^k} + \lambda_1\mathbf{x}|_{\mathbf{x}=\mathbf{x}^k} \\ &= \sum_{j=1}^{N_{img}} \alpha_j^k \mathbf{A}_j^H\left[\left(|\mathbf{A}_j\mathbf{x}|^2 - I_j + \frac{I_j - (\mathbf{A}_j\mathbf{x})^2}{1+\lambda}\right)\odot(\mathbf{A}_j\mathbf{x})\right]|_{\mathbf{x}=\mathbf{x}^k} + \lambda_1\mathbf{x}|_{\mathbf{x}=\mathbf{x}^k}.\end{aligned} \tag{14}$$

Here, the corresponding weighted item and λ_1 will be comparatively low, thereby diminishing the contribution of the derivative of $f(\mathbf{x})$ and and preventing the degeneration of the optimization due to measurement noise. Then, the updating rule can be expressed using the gradient descent technique

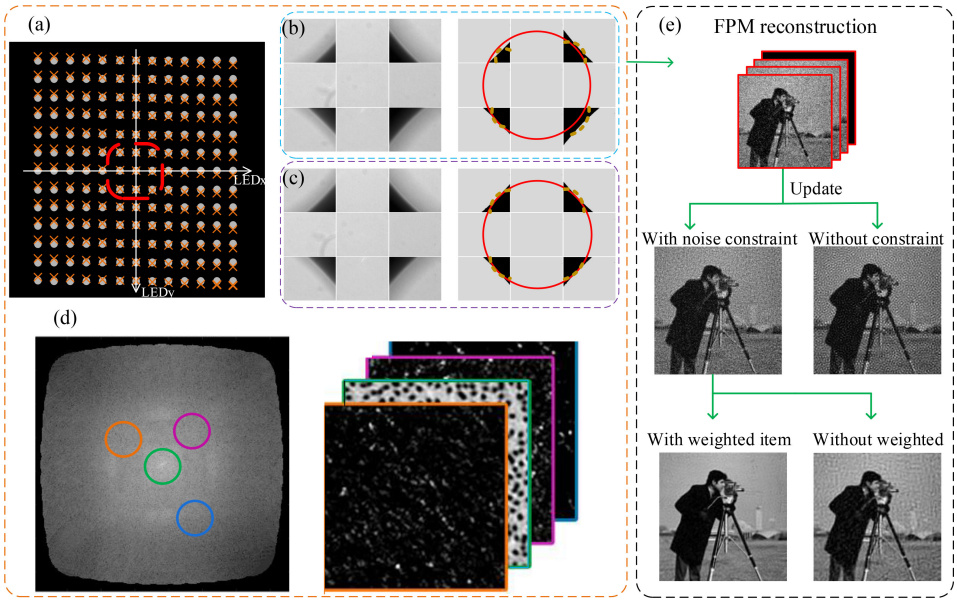

Fig. 2. Preprocessing by BFL and FPM reconstruction. (a) The ideal and misaligned positions of the LED matrix. (b) The images captured by 3×3 LEDs and the corresponding boundaries of the bright and dark fields with the misaligned LED matrix. (c) The same images with BFL correction. (d) The updated spectrum and the images corresponding to different positions of the LED matrix. (e) The advantage and comparison between the proposed scheme and traditional scheme.

as Eq.6 based on Eq.14.

$$\mathbf{x}^{k+1} = \mathbf{x}^k - \mu \frac{\partial f}{\partial \mathbf{x}^*}|_{\mathbf{x}=\mathbf{x}^k}. \tag{15}$$

Similar to the WF and TPWF approaches, the gradient descent step size μ can be estimated as

$$\mu = \frac{\min(1 - e^{-k/k_0}, \mu_{\max})}{m}, \tag{16}$$

where $k_0 = 330$ and $\mu_{\max} = 0.4$ are set because they work well under these settings and offer faster convergence [31].

Recently, our Group has proposed a bright field localization (BFL) preprocessing algorithm [33] that can correct the position of the entire LED matrix. Hence, BFL is utilized before the implementation of CWWFP reconstruction in the experiment. We use 3×3 LEDs to align the LED array in this scheme, as shown in Fig. 2(a). In Fig. 2(b), the corresponding images are asymmetrical, while the boundary of images in Fig. 2(c) nearly constitutes a circle. Fig. 2(e) shows the effect of using the noise constraint and weighted item with the above derivations, and the proposed CWWFP algorithm is introduced as follows. Similar to the conventional AP algorithm, the spatial spectrum of the LR image captured under on-axis illumination is set as the initialization HR spectrum $\mathbf{x}^{(0)}$.

It is worth mentioning that, in our scheme, the weighted item is determined in one iteration. Therefore, the proposed algorithm does not require any additional computational costs. Moreover, by applying the noise relaxation constraint, weighted item and correction term, unknown sources of noise can be corrected, and a more precise reconstruction can be achieved.

3. Results

3.1 Simulation Results

Before applying the proposed algorithm to actual experimental data, we first validate the performance and advantages of the CWWFP scheme using simulations. Raw LR complex images are

Algorithm 1: CWWFP.

Require: $\{I_j\}$, $\{\mathbf{A}_j\}$, α, λ, λ_1, μ;
$\{I_j\}$: captured LR images
$\{\mathbf{A}_j\}$: linear transform matrix
α: adaptive weighted item
λ: constraint item
λ_1: correction term
μ: gradient descent step size
η: the parameter
Ensure: the reconstructed HR complex image $\mathbf{x}$;
Step 1: Preprocessing
Step 2: Initialization
1: Set the initial HR complex spectrum $\mathbf{x}^0$ (initial intensity estimate is the LR image captured under on-axis illumination and the initial phase estimate is zero);
2: Set the initial α^0;
3: Set λ, λ_1;
4: $k = 0$;
Step 3: Calculate
5: Calculate noise relaxation constraint as shown in Eq.10;
6: **for** $k = 0$ to $N_{iteration}$ **do**
7: Calculate the gradient descent step size μ;
8: **for** $j = 1$ to N_{img} **do**
9: Calculate the weighted item α_j^k as shown in Eq.12;
10: Calculate the updated $\mathbf{A}_j\mathbf{x}^{(k+1)}$ as shown in Eq.14;
11: $j = j + 1$;
12: **end for**
13: Complete the $\mathbf{x}^{k+1}$ in one iteration;
14: $k = k + 1$;
15: **end for**
16: Update the estimation $\mathbf{x}$ in all iterations;
17: $\mathbf{x}$ is the recovered HR spatial spectrum. Obtain complex image through the inverse Fourier transform of $\mathbf{x}$.

created from HR 512×512 pixel images based on the parameters of an experimental FPM platform with an incident light wavelength of 629 nm, a $4\times$ objective lens with an NA of 0.13 and a CMOS imaging sensor (2160×2560) with a pixel size of 6.5 μm. Here, we simulate a 13×13 LED array with a spacing of 8.128 mm between adjacent LEDs providing angle-varied illuminations, and the distance between the sample and LED array is 98 mm. To study the performance of the proposed algorithm, we apply the conventional Gerchberg-Saxton, WFP, TPWFP and proposed algorithm to the simulated data with varying levels of noise, including Poisson, Gaussian and speckle noise. All four methods are implemented using Matlab 2016b on an Intel i7-6700K CPU with 16 GB DDR4 memory and a 64-bit Windows 10 operating system. To evaluate the reconstruction performance of the above mentioned methods, we utilize the relative error (RE), which indicates the similarity between the original HR complex image and the reconstructed results.

Based on the above specifications, we first apply the new scheme to the simulated data with varying levels of noise to verify its validity. The raw intensity and phase images are shown in Fig. 3(a). The standard deviation (std) of the additive noise ranges from 0.002 to 0.008 with an interval of 0.002 and 300 iterations. The results are shown in Fig. 3 and Table 1. When the level of Gaussian noise is large, the WFP algorithm cannot extract useful information from the noisy data, and the TPWFP uses the truncated Poisson model, while the proposed CWWFP technique can avoid any negative influence from the noise on the final reconstruction. These results clearly

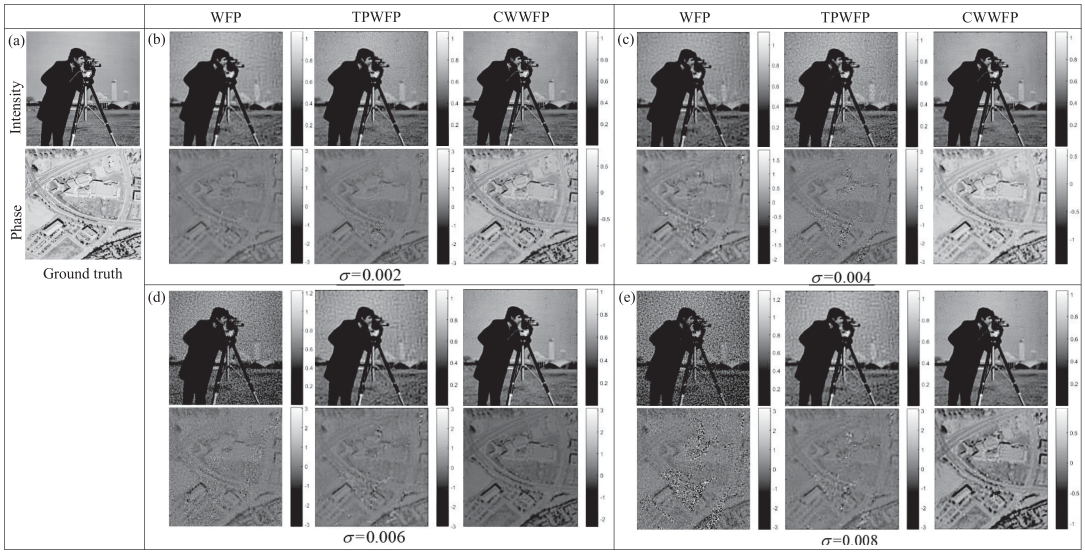

Fig. 3. The comparison results with different levels of simulated Gaussian noise using the WFP, TPWFP and CWWFP algorithms. **The copyright of the cameraman image is held by the Massachusetts Institute of Technology.**

TABLE 1
Comparison of the Res Among the State-of-the-Art Algorithms

σ	0.002	0.004	0.006	0.008
RE(WFP)	0.20100	0.2075	0.2400	0.2549
RE(TPWFP)	0.2034	0.2089	0.2183	0.2238
RE(CWWFP)	0.1257	0.1428	0.1540	0.1614

demonstrate that the proposed CWWFP approach can effectively reconstruct both the intensity and the phase information. In addition, as the noise level increases, the reconstruction quality scarcely degenerates.

Next, we add Poisson noise, Gaussian noise and speckle noise independently and compare the CWWFP technique with the three above mentioned state-of-the-art algorithms to reveal their advantages and disadvantages. As shown in Fig. 4, the std of the Poisson noise is created randomly, while those of the Gaussian and speckle noise are 0.01 and 1, respectively. Gaussian noise often occurs during image acquisition because of defective illumination and sensor noise, and speckle noise represents a type of random scattering from the interior of the basic resolution unit.

From the results illustrated in Fig. 4, it is obvious that the conventional Gerchberg-Saxton method can obtain only the recovered intensity images, while the phase information is distorted; in addition, it is not robust for different types of noise. Under Gaussian noise and speckle noise, some speckles are observed in the recovered intensity images. The WFP algorithm can perform well in the presence of Gaussian noise, as it benefits from the simulation of an additive noise model. However, when the noise level is large, WFP cannot extract useful information from the noisy data. Furthermore, as shown in Fig. 4(d1)–(d3) and Fig. 4(e1)–(e3), the TPWFP and CWWFP algorithms, which are effective at reconstructing both the intensity and the phase information, outperform the other two methods. Nevertheless, due to the accurate Poisson noise model of the TPWFP algorithm, its performance is not as good as expected under Gaussian noise and speckle noise. In contrast, CWWFP performs better than these other three methods; the results reconstructed with the proposed method using these simulated data exhibit a higher quality. Moreover, the details in the intensity images are rich, and there is less noise in the background; this is because we introduce a noise relaxation

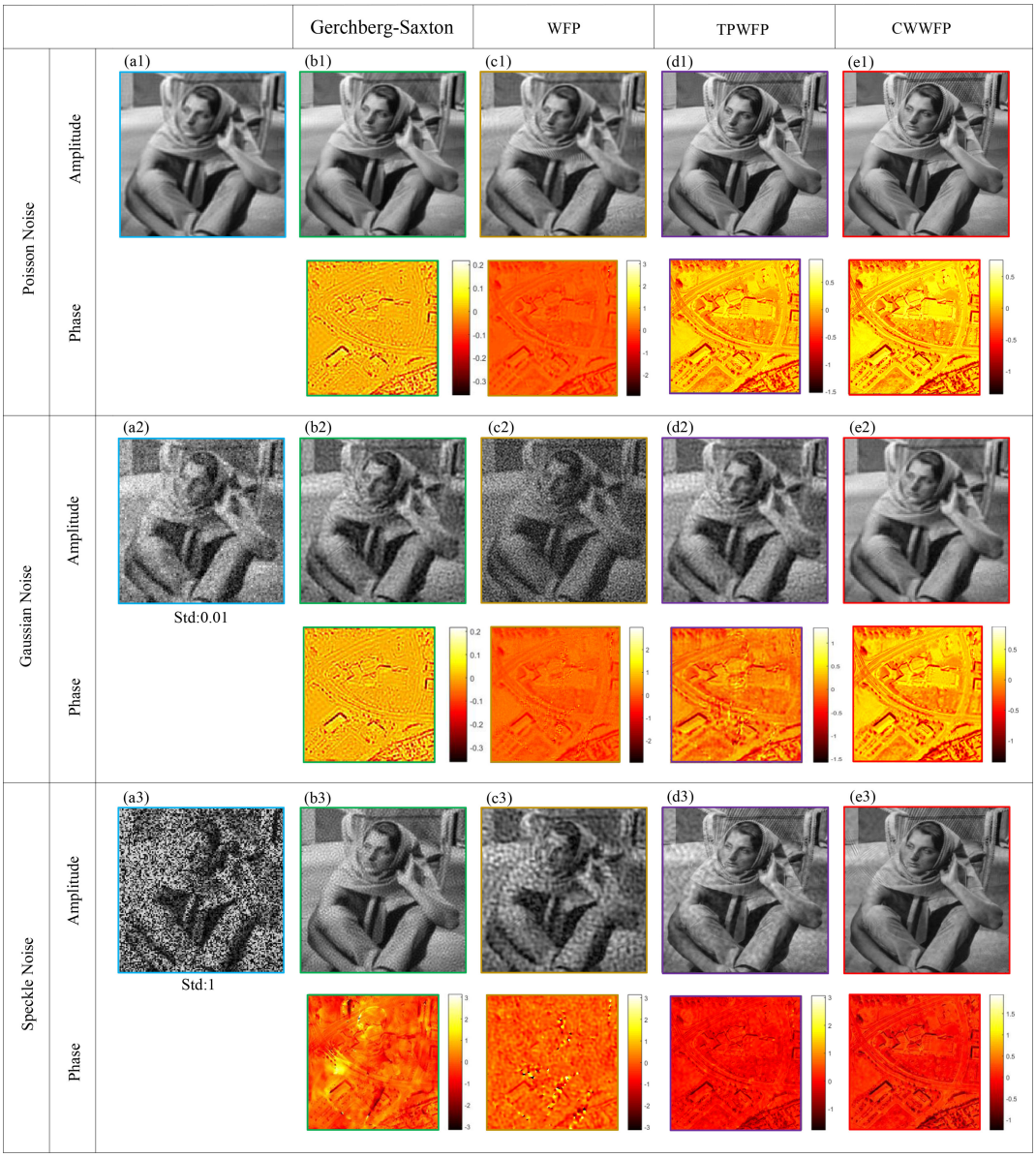

Fig. 4. Reconstructed results under three types of noise using four methods. (a1)–(a3) The LR images under Poisson, Gaussian and Speckle noise. (b1)–(b3), (c1)–(c3), (d1)–(d3) and (e1)–(e3) The reconstructed intensity and phase images using the Gerchberg-Saxton, WFP, TPWFP and CWWFP algorithms, respectively. **The copyright of the intensity image is held by the Signal Compression Lab, University of California.**

constraint into the Wirtinger gradient descent framework that takes both a Poisson model and a Gaussian model into account. In addition, an adaptively calculated weighted item is proposed in this scheme to search for a better result. In conclusion, while the noise within an FPM system can strongly affect the reconstruction quality, the CWWFP technique can successfully reconstruct the images. The simulated results illustrate the robustness of CWWFP to different types of noise.

Furthermore, Fig. 5(a) lists a table showing the REs of recovered images subjected to Poisson noise using the above methods. The quality of the reconstructed image using CWWFP is significantly improved, as shown in Fig. 5(a). We also compare the convergence of the four methods used in this work under Gaussian noise and speckle noise, as shown in Fig. 5(b) and

(a)

	Relative error
GS	0.1853
WFP	0.2068
TPWFP	0.1469
CWWFP	0.1445

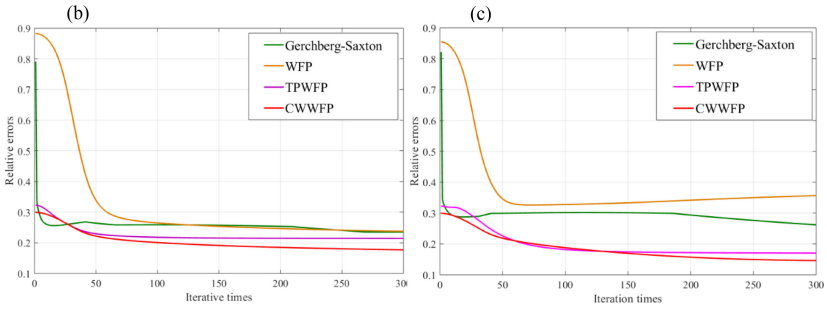

Fig. 5. Table of the REs and curves with different types of noise using the four methods. (a) The RE values of the reconstructed results using four methods under Poisson noise. (b)–(c) The RE curves of the reconstructed results with different iterations under Gaussian noise (b) and speckle noise (c).

Fig. 5(c), respectively. Obviously, the CWWFP technique achieves a better performance, and the RE is less than those of the other methods, but the proposed scheme requires more iterations than the Gerchberg-Saxton method. The criteria curves indicate that the FPM reconstruction can successfully obtain good results after introducing an adaptively calculated weighted item, a noise relaxation constraint and a regularization parameter into the Wirtinger gradient descent framework.

3.2 Experimental Results

Next, to verify the validity of the CWWFP technique, we experimentally compare this scheme with the Gerchberg-Saxton, WFP and TPWFP algorithms based on a real FPM platform, as shown in Fig. 1(a). The parameters in real system setup are the same as those in the simulation. The scientific CMOS (sCMOS) camera was used to record these LR images, and the custom-made LED array was controlled by the Arduino circuit board. According to the above description, the captured LR images are shown in Fig. 2(d) with an exposure time of 100 ms. In principle, because the illumination from the LED array can be regarded as spherical, the final synthetic NA of this system is the sum of the objective and the illumination with the largest angle (approximately 0.7). BFL is first applied to this new scheme to align the position of the whole LED matrix. The dots in Fig. 2(a) represent the ideal position of the LED array, while the aligned positions of the LEDs are marked with an X. Prior to capturing the LR images, images with and without BFL correction were acquired without a sample in the FPM setup, as shown in Fig. 2(b). The boundaries between the bright and dark fields are shown as orange dotted lines, which are misaligned with the standard red circle. Thus, we align the LED array manually to adjust the edge points into a circle whose centre is also approximately the middle of the LR images captured in the bright field. As a result, the overall positional misalignment of the LED matrix can be corrected simply. It is worth mentioning that we adjust the LED array manually only to correct obvious errors in the position of the LEDs to evaluate the effects of suppressing noise utilizing CWWFP.

First, we utilize the United States Air Force (USAF) target and capture a sequence of 13×13 LR images to compare the modified algorithm with the Gerchberg-Saxton, WFP and TPWFP methods. The reconstructed USAF target images are shown in Fig. 6. Fig. 6(a) represents the LR image of the full FOV and a small region of interest (ROI) with a magnified 200×200 pixels, as shown in Fig. 6(b1). Fig. 6(c1), (d1) and (e1) show the recovered intensity images using the Gerchberg-Saxton, WFP and TPWFP methods, respectively, and Fig. 6(f1) shows results using the proposed optimized denoising method. In the results generated by the Gerchberg-Saxton method, most of the details are subtracted, and the edge information is blurry. We can also easily observe that WFP corrugates the recovered intensity image. In addition, the reconstruction results using TPWFP suffer from blurriness due to the Poisson-truncated Wirtinger gradient. In contrast, CWWFP obtains better reconstructed results with more image details and a higher contrast. Fig. 6(b2)–(f2) illustrate the intensity line traces of the USAF target corresponding to Fig. 6(b1)–(f1); it is obvious that the intensity line trace in Fig. 6(f2) has a higher contrast. Although all of these FPM reconstruction

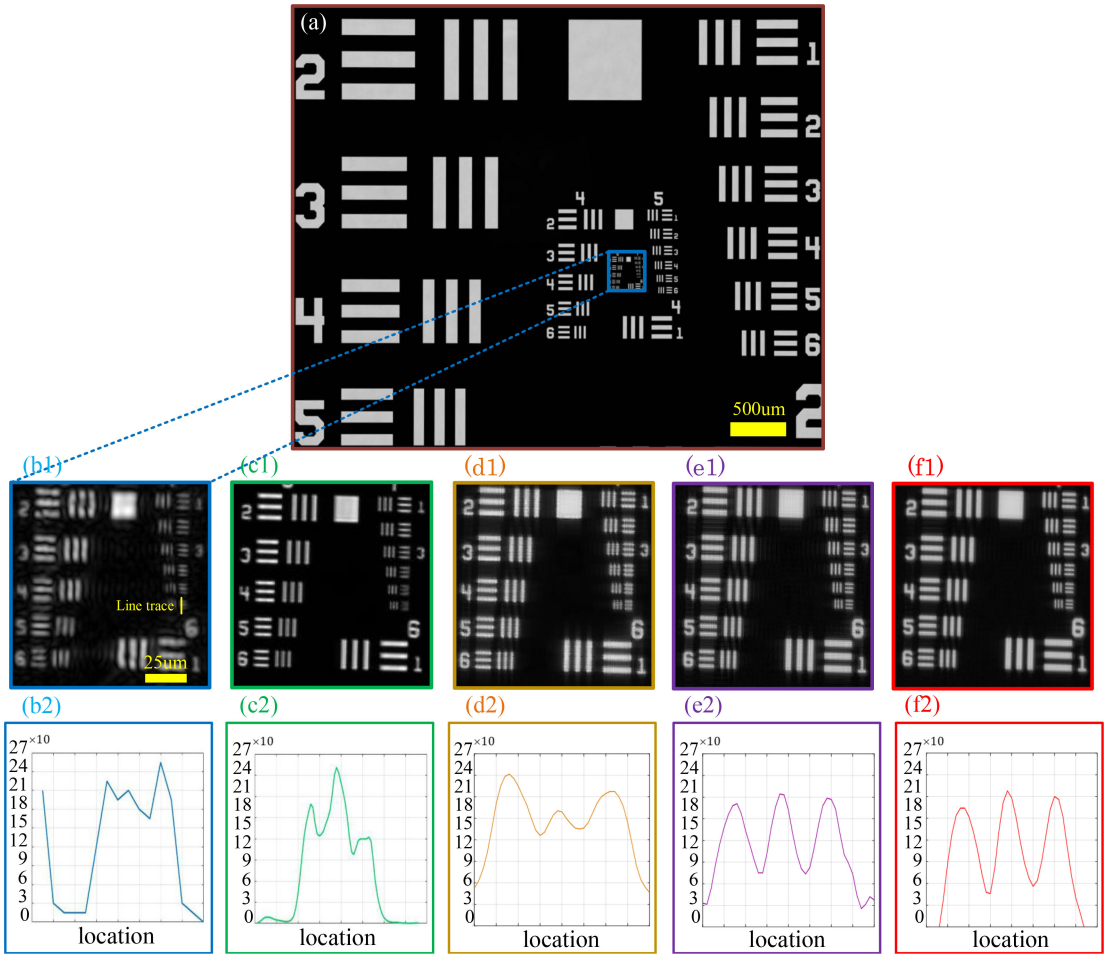

Fig. 6. Experimental results of the USAF target. (a) The FOV of the USAF target image. (b1) The enlarged ROI. (c1)–(f1) The recovered high-resolution intensities with Gerchberg-Saxton, WFP, TPWFP and CWWFP methods respectively. (b2)–(f2) The pixels contrast curves of the intensity line traces corresponding to (b1)–(f1).

algorithms can improve the resolution compared with the raw image, better reconstructed results and a higher resolution can be achieved by using CWWFP, which suffers from less noise. In summary, the proposed CWWFP technique outperforms the other methods with less background noise, higher image contrast and more image details.

Finally, we compare the CWWFP algorithm with the three state-of-the-arts using a blood smear. In addition, we also verify that FPM can achieve synthetic aperture imaging in this experiment. To obtain a colour image of the blood smear, we use red (629 nm), green (520 nm) and blue (465 nm) LED illuminations to capture LR images and separately reconstruct HR complex images, after which we combine these reconstructions into the final colour image. Fig. 7(a) presents a wide FOV colour image of the blood smear, while Fig. 7(b) shows a magnified ROI obtained from a conventional microscope setup with a $4\times$ objective lens with an $NA = 0.13$. By utilizing the four FPM reconstruction algorithms, the same sub-regions using the Gerchberg-Saxton and CWWFP methods with a synthetic $NA = 0.7$ are shown in Fig. 7(c) and Fig. 7(d), respectively. The recovered intensity image using CWWFP contains more details and a higher resolution; this result is the same as the effect of using a $40\times$ objective lens with an $NA = 0.7$, as shown in Fig. 7(a1). The difference between these two algorithms is the size of the FOV; as shown in Fig. 7(a), the small region marked with a blue dashed window is the FOV under a $40\times$ objective lens. Fig. 7(b)–(d), the centre of

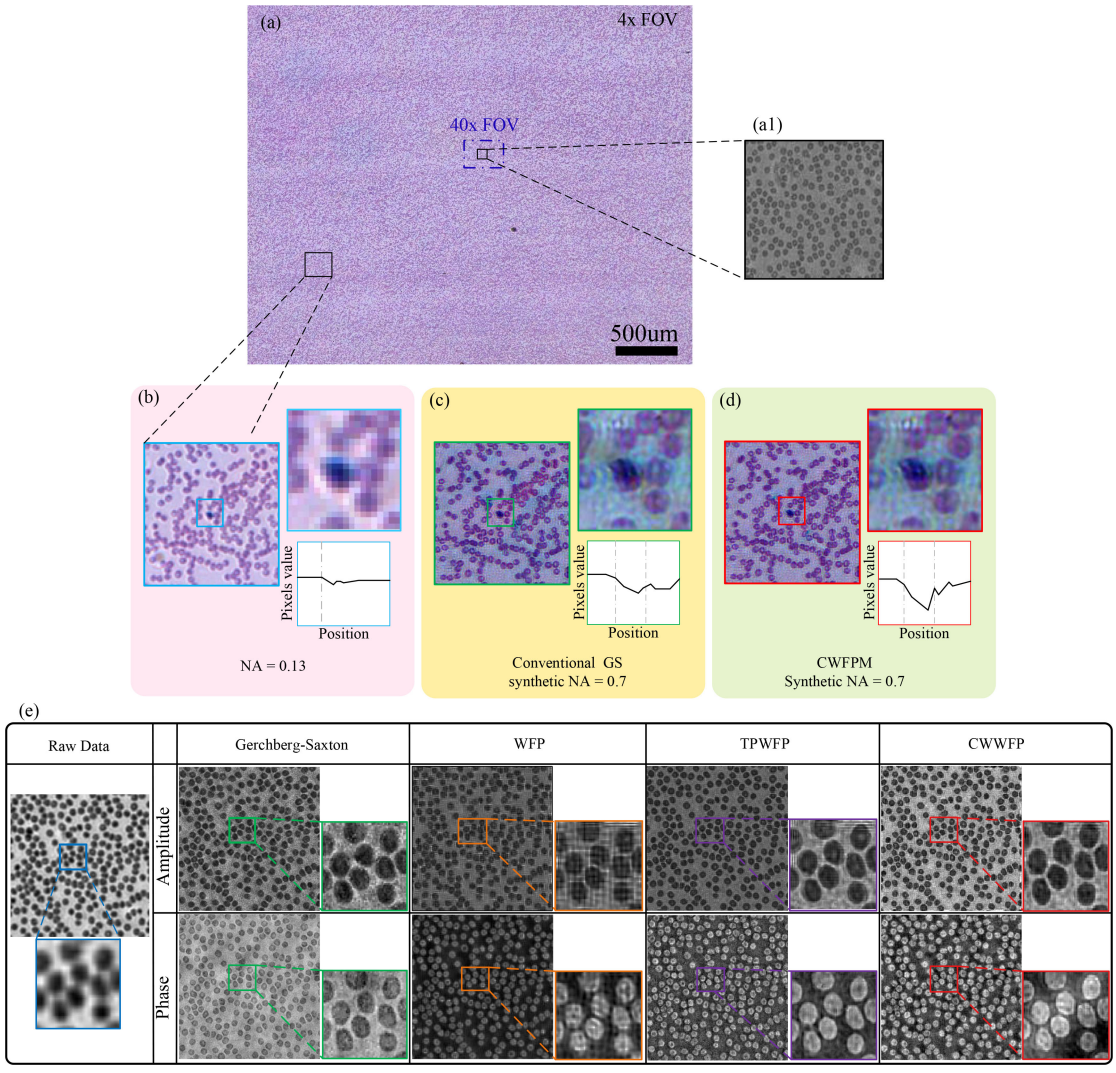

Fig. 7. Imaging and reconstructed results of conventional microscope and FPM reconstruction algorithms for blood smear. (a) The FOV of the incoherent microscope image using a 4 × 0.13NA objective lens. (a1) The enlarged sub-region using a 40 × 0.7NA objective lens. (b)–(d) Imaging and reconstructed results of the same sub-region of Fig. 7(a) using conventional 0.13NA microscopy, Gerchberg-Saxton and CWWFP synthetic 0.7NA methods. And the curves of changes of the white cells' edge. (e) The raw data and reconstruction results by the three state-of-the-arts and the proposed CWWFP.

the magnified ROI is a coloured white cell; this image is clearly reconstructed using CWWFP with an objective lens with $NA = 0.7$, and the changes in the boundaries of the blue cell are shown in the curves. Then, we choose another region to compare the reconstructed results using the four methods as shown in Fig. 7(e). From the reconstructed results in Fig. 7(e), it is obvious that the Gerchberg-Saxton method can improve the resolution of the LR image. However, most of the noise in the background still exists, significantly producing fluctuations in the background of the reconstructed images. In contrast, the results using the WFP scheme, the various types of noise are nearly removed, and the resolution is also increased; however, the results has corrugated appearance originating from Poisson noise within the system, and thus, the contrast of the results is low. The TPWFP and CWWFP algorithms obtain better results with regard to the resolution, and they can remove the fluctuations in the background. Nevertheless, the contrast with the CWWFP application is higher, better saturation and more high frequency information. Furthermore, the

quality of the recovered phase image using CWWFP is better in terms of the resolution due to the application of the adaptively calculated weighted item and the noise relaxation constraint in the WF gradient.

4. Discussion

In this paper, we have developed and tested an optimized denoising method. The main purpose of this scheme is to reduce different types of noise and search for the optimization solution. To analyse the robustness of the CWWFP techniques, different types of noise common within real system setups are generated in simulated LR images; the results indicate that the proposed technique is more efficient and can achieve better reconstructed results than existing algorithms. Different from the conventional FPM and Wirtinger gradient methods, CWWFP adopts a variable weighted item that can be regarded as a truncated gradient to control the gradient descent direction and obtain the optimization solution. Moreover, the high-quality recovered intensity and phase images through these simulations and experiments using the Gerchberg-Saxton, WFP, TPWFP and CWWFP methods have been demonstrated. The simulation and experimental results all show that CWWFP can accurately reduce the interference due to various types of noise while significantly improving the reconstruction quality of HR complex images and can converge more quickly than the conventional WF algorithm. In addition, CWWFP can be applied in other imaging systems as a consequence of its robustness for different types of noise.

However, in spite of the high quality of the reconstructed HR complex images, the proposed CWWFP scheme cannot recover HR images with fewer iterations than the Gerchberg-Saxton algorithm, which will limit the application of CWWFP in real-time observations. In future research, the combination of the CWWFP method with a multiplexed coded illumination algorithm may overcome these weaknesses. Moreover, because the convex optimization method has recently been verified for phase retrieval, incorporating the convex optimization model into the original WF method may provide a novel method for resolving the problem of integral edge blur.

Acknowledgment

The authors would like to thank the anonymous reviewers for their valuable suggestions.

References

[1] H. M. Faulkner and J. M. Rodenburg, "Movable aperture lensless transmission microscopy: A novel phase retrieval algorithm," *Phys. Rev. Lett.*, vol. 93, no. 2, 2004, art. no. 023903.
[2] J. Sun, Q. Chen, Y. Zhang, and C. Zuo, "Efficient positional misalignment correction method for Fourier ptychographic microscopy," *Biomed. Opti. Exp.*, vol. 7, no. 3, pp. 1336–1350, Apr. 2016. [Online]. Available: https://www.osapublishing.org/abstract.cfm?URI=boe-7-4-1336
[3] J. M. Rodenburg and H. M. L. Faulkner, "A phase retrieval algorithm for shifting illumination," *Appl. Phys. Lett.*, vol. 85, no. 20, pp. 4795–4797, 2004.
[4] A. R. Cohen, F. L. F. Gomes, B. Roysam, and M. Cayouette, "Computational prediction of neural progenitor cell fates," *Nature Methods*, vol. 7, no. 3, pp. 213–218, 2010.
[5] T. R. Hillman, T. Gutzler, S. A. Alexandrov, and D. D. Sampson, "High-resolution, wide-field object reconstruction with synthetic aperture Fourier holographic optical microscopy," *Opt. Exp.*, vol. 17, no. 10, pp. 7873–7892, 2009.
[6] A. M. Maiden and J. M. Rodenburg, "An improved ptychographical phase retrieval algorithm for diffractive imaging," *Ultramicroscopy*, vol. 109, no. 10, pp. 1256–1262, 2009.
[7] P. Gao, G. Pedrini, and W. Osten, "Structured illumination for resolution enhancement and autofocusing in digital holographic microscopy," *Opt. Lett.*, vol. 38, no. 8, pp. 1328–1330, 2013.
[8] A. E. Tippie, A. Kumar, and J. R. Fienup, "High-resolution synthetic-aperture digital holography with digital phase and pupil correction," *Opt. Exp.*, vol. 19, no. 13, pp. 12027–12038, 2011.
[9] G. Zheng, R. Horstmeyer, and C. Yang, "Wide-field, high-resolution Fourier ptychographic microscopy," *Nature Photon.*, vol. 7, no. 9, pp. 739–745, Jul. 2013. [Online]. Available: http://arxiv.org/abs/1605.09782 http://www.nature.com/doifinder/10.1038/nphoton.2013.187
[10] R. A. Gonsalves, "Phase retrieval and diversity in adaptive optics," *Opt. Eng.*, vol. 21, no. 5, pp. 829–832, 1982.
[11] J. R. Fienup, "Phase-retrieval algorithms for a complicated optical system," *Appl. Opt.*, vol. 32, no. 10, pp. 1737–1746, 1993.

[12] M. Guizar-Sicairos and J. R. Fienup, "Phase retrieval with transverse translation diversity: A nonlinear optimization approach," *Opt. Exp.*, vol. 16, no. 10, pp. 7264–7278, 2008.
[13] S. Pacheco, B. Salahieh, T. Milster, J. J. Rodriguez, and R. Liang, "Transfer function analysis in epi-illumination Fourier ptychography," *Opt. Lett.*, vol. 40, no. 22, pp. 5345–5346, 2015.
[14] G. Zheng, "Breakthroughs in Photonics 2013: Fourier Ptychographic Imaging," *IEEE Photon. J.*, vol. 6, no. 2, Apr. 2014, Art. no. 0701207.
[15] K. Guo, S. Dong, and G. Zheng, "Fourier ptychography for brightfield, phase, darkfield, reflective, multi-slice, and fluorescence imaging," *IEEE J. Sel. Topics Quantum Electron.*, vol. 22, no. 4, Jul./Aug. 2016, Art. no. 6802712.
[16] J. Chung, X. Ou, R. P. Kulkarni, and C. Yang, "Counting white blood cells from a blood smear using Fourier ptychographic microscopy," *PLoS ONE*, vol. 10, no. 7, pp. 1–10, 2015.
[17] A. Williams *et al.*, "Fourier ptychographic microscopy for filtration-based circulating tumor cell enumeration and analysis," *J. Biomed. Opt.*, vol. 19, no. 6, 2014, Art. no. 066007.
[18] L. Tian and L. Waller, "3D intensity and phase imaging from light field measurements in an LED array microscope," *Optica*, vol. 2, no. 2, pp. 104–111, 2015.
[19] L. Tian, X. Li, K. Ramchandran, and L. Waller, "Multiplexed coded illumination for Fourier ptychography with an LED array microscope," *Biomed. Opt. Exp.*, vol. 5, no. 7, pp. 2376–2389, 2014.
[20] S. Dong, Z. Bian, R. Shiradkar, and G. Zheng, "Sparsely sampled Fourier ptychography," *Opt. Exp.*, vol. 22, no. 5, pp. 5455–5464, 2014. [Online]. Available: https://www.osapublishing.org/oe/abstract.cfm?uri=oe-22-5-5455
[21] L. Bian, J. Suo, G. Situ, G. Zheng, F. Chen, and Q. Dai, "Content adaptive illumination for Fourier ptychography," *Opt. Lett.*, vol. 39, no. 23, pp. 6648–6651, 2014.
[22] L. Tian, Z. Liu, L.-H. Yeh, M. Chen, J. Zhong, and L. Waller, "Computational illumination for high-speed in vitro Fourier ptychographic microscopy," *Optica*, vol. 2, no. 10, pp. 904–911, 2015. [Online]. Available: https://www.osapublishing.org/abstract.cfm?URI=optica-2-10-904
[23] Z. Bian, S. Dong, and G. Zheng, "Adaptive system correction for robust Fourier ptychographic imaging," *Opt. Exp.*, vol. 21, no. 26, pp. 32400–32410, 2013. [Online]. Available: https://www.osapublishing.org/oe/abstract.cfm?uri=oe-21-26-32400
[24] X. Ou, G. Zheng, and C. Yang, "Embedded pupil function recovery for Fourier ptychographic microscopy," *Opt. Exp.*, vol. 22, no. 5, pp. 4960–4972, 2014.
[25] J. Zhang, T. Xu, X. Wang, S. Chen, and G. Ni, "Fast gradational reconstruction for Fourier ptychographic microscopy," *Chin. Opt. Lett.*, vol. 15, no. 11, p. 111702, 2017, Art. no. 111702. [Online]. Available: http://www.opticsjournal.net/Abstract.htm?id=OJ170930000081B8EaHd
[26] C. Zuo, J. Sun, and Q. Chen, "Adaptive step-size strategy for noise-robust Fourier ptychographic microscopy," *Opt. Exp.*, vol. 24, no. 18, pp. 20724–20744, 2016.
[27] X. Ou, R. Horstmeyer, G. Zheng, and C. Yang, "High numerical aperture Fourier ptychography: Principle, implementation and characterization," *Opt. Exp.*, vol. 23, no. 3, pp. 3472–3491, 2015.
[28] R. Horstmeyer, R. Y. Chen, X. Ou, B. Ames, J. A. Tropp, and C. Yang, "Solving ptychography with a convex relaxation," *New J. Phys.*, vol. 17, no. 5, 2015, Art. no. 53044.
[29] L. Bian, J. Suo, G. Zheng, K. Guo, F. Chen, and Q. Dai, "Fourier ptychographic reconstruction using Wirtinger flow optimization," *Opt. Exp.*, vol. 23, no. 4, p. 4856, 2015, Art. no. 4856. [Online]. Available: https://www.osapublishing.org/abstract.cfm?URI=oe-23-4-4856
[30] L. Bian *et al.*, "Fourier ptychographic reconstruction using Poisson maximum likelihood and truncated Wirtinger gradient," *Scientific Rep.*, vol. 6, no. 1, Jul. 2016, Art. no. 27384. [Online]. Available: http://arxiv.org/abs/1603.04746%0Ahttp://dx.doi.org/10.1038/srep27384http://www.nature.com/articles/srep27384
[31] E. Candes, X. Li, and M. Soltanolkotabi, "Phase retrieval via wirtinger flow: Theory and algorithms," *IEEE Trans. Inf. Theory*, vol. 64, no. 4, pp. 1985–2007, Apr. 2015.
[32] Z. Yuan and H. Wang, "Phase retrieval via reweighted Wirtinger flow," *Appl. Opt.*, vol. 56, no. 9, pp. 2418–2427, 2017.
[33] J. Zhang, T. Xu, J. Liu, S. Chen, and X. Wang, "Precise brightfield localization alignment for Fourier ptychographic microscopy," *IEEE Photon. J.*, vol. 10, no. 1, Feb. 2018, Art. no. 6900113. [Online]. Available: http://ieeexplore.ieee.org/document/8166728/